Official journal of the JHL 2689-9620
www.light-am.com

Article Open Access

Multivariate relationships between microstructure evolution and strengthening mechanisms in laser powder bed fusion of Al-Mn-Sc alloy: towards improved fatigue performance

Huaping Tang[1], Chaofeng Gao[1], Shiheng Zhang[1], Xiaojing Xiong[1], Sheng Cao[2], Xiaopeng Wu[3], Yunjie Bi[1] and Jeremy Heng Rao[1,*]

Abstract

The effects of direct aging treatment (at 300 ℃ for 5 hours) on selective laser melted (SLMed) Al-4.5Mn-1.5Mg-0.9Sc-0.2Zr alloy were investigated in this work, with the microstructure, fatigue behaviors, and fracture characteristics examined to determine the primary cause of fatigue crack source. The results revealed that the microstructure of the investigated alloy comprised fine equiaxed and columnar grains. Upon aging treatment, a significant number of nano-scaled Al_3(Sc, Zr) precipitates were dispersed within the grains, leading to a substantial increase in strengths. The yield strength improved from 431 MPa to 568 MPa, representing an increase of more than 32%, while the fatigue strength improved from 180 MPa to 220 MPa after aging treatment. Nevertheless, the fracture toughness decreased significantly from $25.1\ \mathrm{MPa}\cdot\sqrt{\mathrm{m}}$ to $12.3\ \mathrm{MPa}\cdot\sqrt{\mathrm{m}}$. The results of the fatigue fracture characteristics indicate that the Mn-rich phase and the formation of defects such as pores and poor powder fusion are the sources of fatigue cracking. Although direct aging treatment can significantly increase the yield strength, decrease the rate of fatigue crack propagation, and thus improve the fatigue performance, it deteriorates the fracture toughness, and thus shortens the fatigue life of the alloy as well.

Keywords: Selective laser melting, Al-Mn-Sc alloys, High-cycle fatigue

Introduction

Aluminum alloys are widely utilized in aerospace and automotive industries due to their lightweight, high specific strength, and high specific stiffness as a structural material[1]. In recent years, laser technology has been found in widespread applications in manufacturing, including laser direct writing[2–4] and additive manufacturing. Selective laser melting, as an advanced metal additive manufacturing technique, provides the benefits of substantial design flexibility and quick fabrication of small quantities of complex structural components. This technique offers a new approach for maximizing the lightweight advantage of aluminum alloys. Beside static load components, aluminum

Correspondence: Jeremy Heng Rao (raohengo@jihualab.com)
[1]Institute of Advanced Additive Manufacturing, Ji Hua Laboratory, Foshan, Guangdong, 528200, China
[2]Department of Mechanical Engineering, College of Engineering, Shantou University, Shantou, Guangdong, 515063, China
Full list of author information is available at the end of the article.

alloys are also employed in additive manufacturing for dynamic load components, which have more stringent requirements for strength, toughness, and fatigue performance[5].

The application of aluminum alloys in additive manufacturing is gradually expanding beyond conventional Al-Si alloys to high-strength Al-Cu and Al-Zn-Mg-Cu alloys, and their performance is constantly evolving. Although Al-Si alloys such as AlSi10Mg and AlSi12Mg are currently the primary materials used in SLMed aluminum alloys due to their outstanding formability, their yield strength of less than 350 MPa and elongation of less than 10% still fall behind high-strength aluminum's performance[6]. To address this, the early strategy was to develop aluminum alloys suitable for the SLM technique based on traditional deformed high-strength alloys such as Al-Zn-Mg-Cu and Al-Cu. However, most of them are sensitive to hot cracking because of their wide solidification range. The addition of grain refinements, such as H_2Zr[7], TiB_2[8], and Al_3Zr[9], act as heterogeneous nucleation particles, improving the alloys' solidification cracking resistance by refining their microstructure, but high temperature applications are limited to a certain extent, due to nanoparticle aggregation and thus easier fracture.

During the last few years, a novel high-strength Al-(Mn, Mg)-Sc alloy has been developed through extensive composition optimization and grain refinement techniques. This alloy can be divided into two categories, the Al-Mg-Sc alloys[10,11] and the Al-Mn-Sc alloys[12,13], based on their Mn and Mg content. Sc, a crucial alloying element, gives the alloy excellent SLM formability and high strength characteristics. The addition of a high Sc content (0.6-1.0 wt.%) effectively refines the grains, reduces thermal cracking tendency, and thus enhances 3D printing formability. Furthermore, aging treatment encourages the precipitation of the supersaturated Sc and Zr atoms dissolved in the Al matrix, resulting in the formation of nano-sized precipitated Al_3(Sc, Zr) phase to contribute to an effective strengthening mechanism, giving the alloy high-strength characteristics[14,15].

By comparing the mechanical properties of the Al-(Mn, Mg)-Sc alloy with those of conventional high-strength aluminum alloys prepared by selective laser melting[8,12, 14–20], it can be observed that the yield strength of the conventional high-strength Al alloys is less than 500 MPa, while the comprehensive mechanical properties (yield strength and elongation) of Al-(Mn, Mg)-Sc alloys are significantly superior. The yield strength of Al-Mn-Sc alloys is higher than that of Al-Mg-Sc alloys, with an increase of approximately 60 MPa due to the enhanced solid solution strengthening of Mn[21]. Consequently, the Al-(Mn, Mg)-Sc alloy has emerged as a pivotal 3D printing high-performance Al alloy, offering excellent strength and ductility via direct aging treatment, and exhibiting immense potential in dynamic load component applications. However, reports about the fatigue properties of Al-(Mn, Mg)-Sc alloys are scant[5]. A recent study on the fatigue properties of 3D printed Al-Si alloy demonstrates that simultaneous improvement in the yield strength and fatigue strength of Al-Si alloy is attainable through process optimization of heat treatment, and the fatigue strength of AlSi10Mg alloy can reach 200 MPa[22]. Prior research underscores that direct aging treatment can significantly enhance the tensile properties of Al-(Mn, Mg)-Sc alloy, with promising prospects for simultaneous improvement in the fatigue properties of the alloy[23].

Therefore, this study investigates the microstructural changes and fatigue properties of the Al-4.5Mn-1.5Mg-0.9Sc-0.2Zr alloy fabricated through selective laser melting undergoing direct aging treatment. Furthermore, the causes of fatigue crack initiation were determined by analyzing the fracture surface, and the mechanisms behind the improvement in the alloy's fatigue properties by direct aging treatment was discussed. These research findings provide significant implications for material service life assessment and component design.

Materials and Methods

The Al-4.5Mn-1.5Mg-0.9Sc-0.2Zr alloy powder was prepared through high-speed centrifugal atomization technology by Jihua Laboratory. The powder's particle size distribution was analyzed by the Mastersizer 3000 Malvern laser particle size analyzer, revealing that the D10, D50, and D90 values were 12.4 μm, 33.4 μm, and 61.3 μm, respectively. The powders had a perfect sphericity and a minimal amount of satellite powder, as shown in Fig. 1a. To produce a dense Al-4.5Mn-1.5Mg-0.9Sc-0.2Zr alloy, process parameters were optimized on the EOS M290 equipment. The scanning strategy involves printing square samples through orthogonal testing and selecting the optimal forming parameters for achieving the maximum density. The optimized parameters were as follows: laser power of 313 W, scan speed of 1158 mm/s, scan spacing of 0.12 μm, and layer thickness of 30 μm. Using these optimized parameters, cubic samples (10 mm × 10 mm × 10 mm), tensile and fatigue testing sample, as well as fracture toughness samples were produced, as shown in Fig. 1b. The size of the specimens is displayed in Fig. 1c.

The composition and density are analyzed after detaching the printed sample from the substrate through the application of electric discharge wire (EDW) cutting

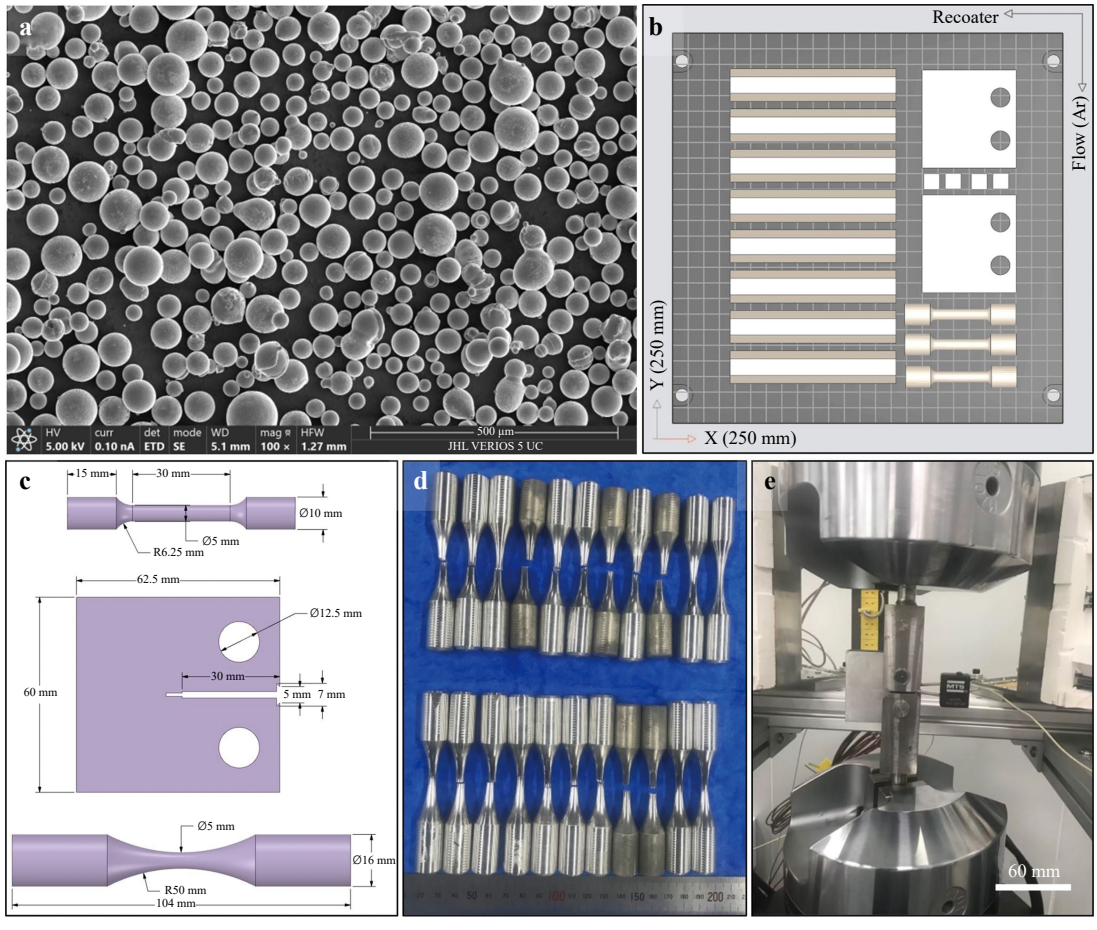

Fig. 1 a Morphology of Al-4.5Mn-1.5Mg-0.9Sc-0.2Zr alloy powder; **b** 3D printed samples; **c** Dimensions of the tensile, fatigue and fracture toughness samples; **d** the fatigue samples after fracture; **e** fatigue and fracture toughness testing equipment.

technique. Initially, ICP has been utilized to determine the sample's composition, and the results are represented in Table 1. The theoretical density has been calculated to be 2.80g/cm^3 based on the composition analysis. The actual density of the cubic sample is assessed through the Archimedes method. The surface of the cubic sample has been polished before conducting density measurements. Finally, the relative density has been estimated to be approximately 99.5% considering the actual density and theoretical density.

The test specimens were categorized into two groups: non-heat-treated and heat-treated. The direct aging heat treatment process involves investigating the alloy's aging hardening behavior at 300 ℃ and determining the peak hardness point as the optimized heat treatment process parameters, namely, aging at 300 ℃ for 5 hours. Thus, the heat-treated specimens underwent treatment at a temperature of 300 °C for a duration of 5 hours. The as-deposited and heat-treated specimens were analyzed for their tensile properties, fatigue strength (as shown in Fig. 1d), and fracture toughness (as depicted in Fig. 1f), respectively. The samples were cut perpendicular to the building direction in accordance with the ASTM E8 standard. Tensile tests were conducted on an electronic universal testing machine manufactured by SUNS Co., Ltd., at a strain rate of 1×10^{-2} s^{-1} at room temperature. Three tensile tests were conducted for each condition to acquire average results. The fracture toughness and fatigue strength tests were carried out on the MTS Landmark 370.10 testing apparatus. The fatigue test parameters were set to a frequency of 30 Hz, an R value of 0.1, and a loading range between 180 MPa and 350 MPa. It should be noted that during fatigue tests the sample that reached 1×10^7 cycles without breakage is considered as the run-out

Table 1 The composition of the as-deposited alloy

Element	Mn	Mg	Sc	Zr	Fe	Si	Al
wt.%	4.65	1.52	0.89	0.20	0.08	0.06	92.60
at.%	2.35	1.73	0.55	0.06	0.04	0.06	95.21

sample, and the corresponding loading stress is determined as the fatigue strength.

The samples intended for observation via OM and SEM microscopy were ground on the 300/500/1000 and 2000 mesh sandpaper, respectively, and then further polished and etched. The metallographic etching solution of choice was Keller's reagent, composed of 95 ml diluted water, 2.5 ml HNO_3, 1.5 ml HCl and 0.5 ml HF, which was left to corrode for a duration of 15 seconds. Examinations of the microstructures were completed in part thanks to both Optical Microscopy (OM, Olympus AX8971) and Scanning Electron Microscopy (SEM, Quanta 400 FEG with Oxford Symmetry EBSD Detector). Precipitates within the alloy were observed using Transmission Electron Microscopy (TEM, FEI Titan Themis 200), and the digital micrograph program was used to calibrate their sites. The procedure for the preparation of these samples is fully outlined in Ref. 6. Additionally, the features associated with both tensile fracture and fatigue fracture, such as fatigue crack sources and fatigue striations, were identified using SEM, and EDS composition detection modules were used to establish the type of fatigue crack source. The calculation method in Ref. 24 is used for the evaluation of the defect size of fatigue crack source, and its value is equal to the square root of the area of fatigue crack source.

Results

Microstructure evolution

Fig. 2 illustrates the microstructures of the as-deposited alloy in the longitudinal and transverse directions. The microstructure (Fig. 2b, d) shows typical sintered strips in the transverse direction, while the longitudinal direction comprises a fish-scale stacked structure (Fig. 2a, c). Furthermore, the microstructure revealed varying features at the edge and the core of the molten pool. As observed in Fig. 2e, f, in the core of the molten pool, the second phases located around the grain boundaries promote the formation of columnar corrosion pits. Conversely, at the edge of the

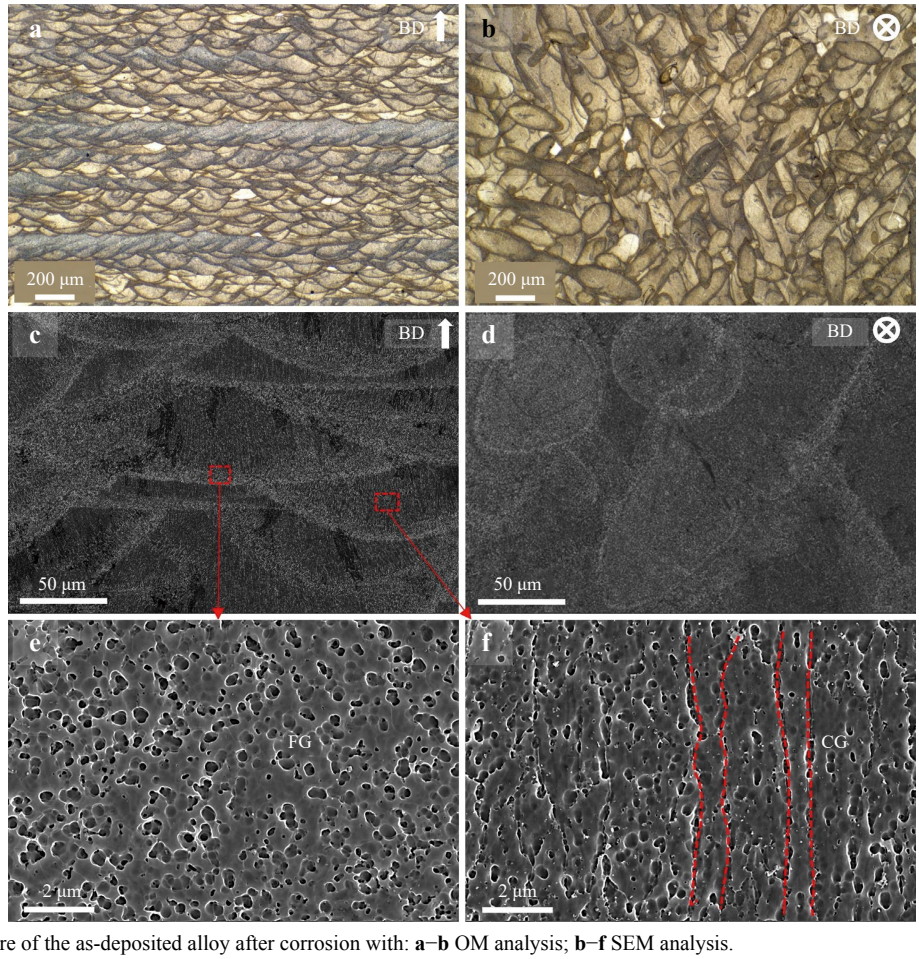

Fig. 2 Microstructure of the as-deposited alloy after corrosion with: **a**–**b** OM analysis; **b**–**f** SEM analysis.

molten pool, the corrosion pits are evenly distributed and exhibit a morphology similar to that of the Al-Mg-Sc-Zr alloy after corrosion[25]. This is attributed to the equiaxed grain structure at the edge of the molten pool and columnar grain structure at its center, wherein the second phase is distributed along the grain boundaries and exhibits morphology as shown in Fig. 2e, f. These second phases would fall off and form the corrosion pits, with sizes ranging between 100 and 200 nm.

The microstructures of the as-deposited alloy was observed by TEM, as shown in Fig. 3. It is evident that the microstructure comprises equiaxed and columnar grains, with some secondary phases located around the boundaries. These small secondary phases are distributed both within the grains and at the grain boundaries. EDS detector was employed to test the composition of the secondary phases in TEM, and the results are illustrated in Fig. 3. The elemental analysis depicts that these phases at the grain boundaries are Mn-rich and Sc/Zr-rich. Furthermore, Sc, Mn and other elements exhibit high contents in the grains. The average composition in this region is Al-2.33Mn-2.07Mg-0.54Sc-0.10Zr (at.%), which is quite close to the alloy composition (Al-2.35Mn-1.73Mg-0.55Sc-0.06Zr, at.%). This denotes that the composition is uniformly distributed.

EBSD and TEM characterization methods were

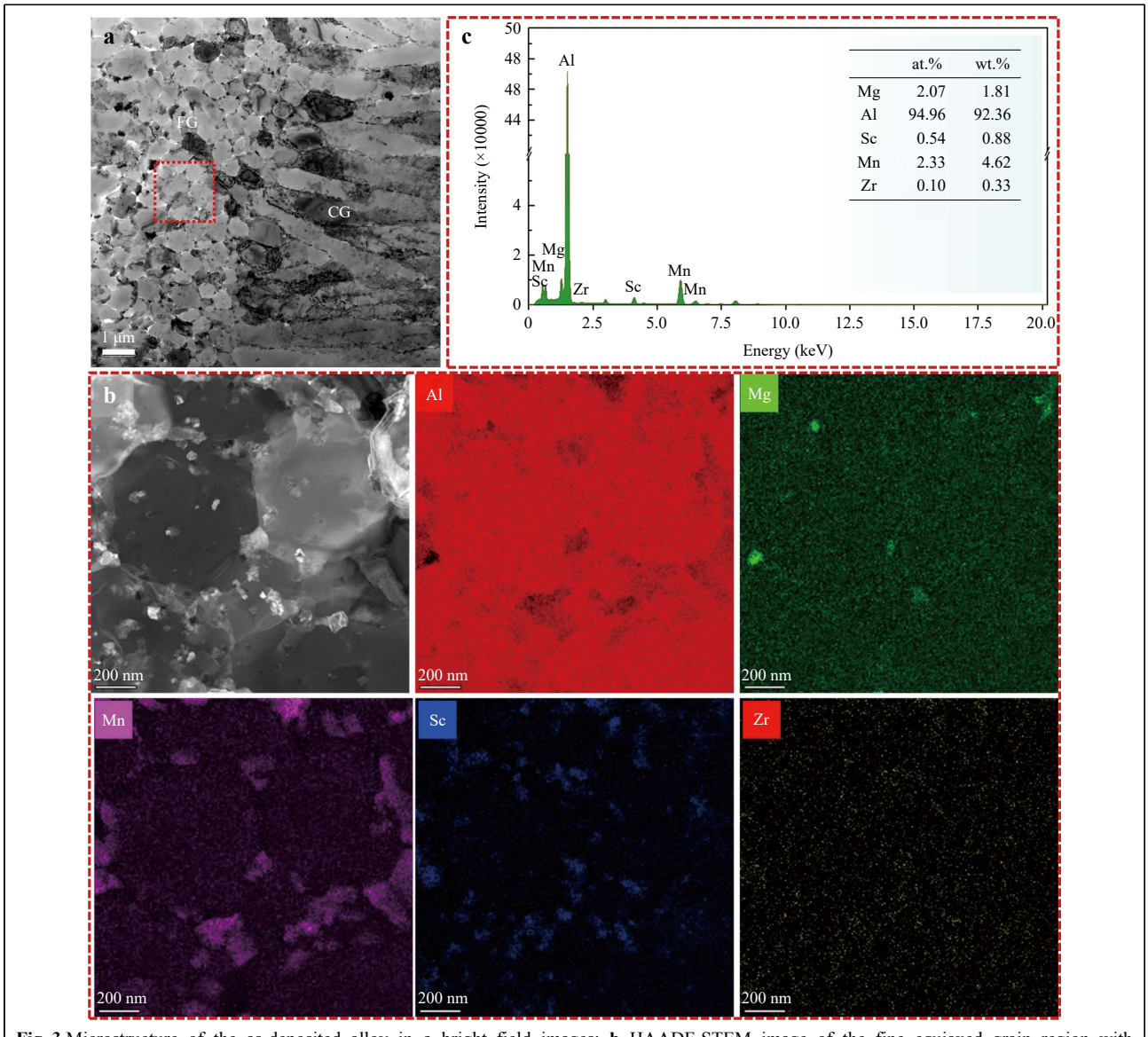

Fig. 3 Microstructure of the as-deposited alloy in **a** bright field images; **b** HAADF-STEM image of the fine equiaxed grain region with corresponding STEM-EDX elemental mapping of Al, Mg, Mn, Sc and Zr; **c** composition in the corresponding area.

employed to observe the microstructure of the direct aged sample, and the results are depicted in Fig. 4. Based on the test results of EBSD, the microstructure of the alloy comprises columnar grains (coarse grains) at the center of the molten pool and equiaxed grains (fine grains) at the edge of the molten pool. The grain size distribution and the average diameter were both determined using the method of equivalent circle area. The results are presented in Fig. 4e, with an average equivalent circle diameter of 2.01 μm. Additionally, the proportion of fine equiaxed grains and columnar grains was evaluated using the EBSD results, with 43% and 57% respectively. Previous research has shown that the fatigue strength of 3D-printed high-strength aluminum alloy is closely related to the size of the columnar grains, and the length of the columnar grain can be used to evaluate the intrinsic critical crack defects[24]. Using the equivalent ellipse calculation method, the long axis diameter of columnar grains within the 5-30 μm range was determined, and the results are presented in Fig. 4f. The average size of columnar grains, with a size distribution in the top 20%, was calculated to be 15.67 μm. Moreover, due to the fine size of the equiaxed grains, it can be challenging to discern their size using EBSD. TEM was employed to investigate the equiaxed grains. The findings reveal that the size of the equiaxed grains is relatively uniform, with a diameter of approximately 483 nm. Furthermore, it is evident that some secondary phases are present near the grain boundary, forming a network-like pattern.

After being subjected to heat treatment at 300 ℃ for

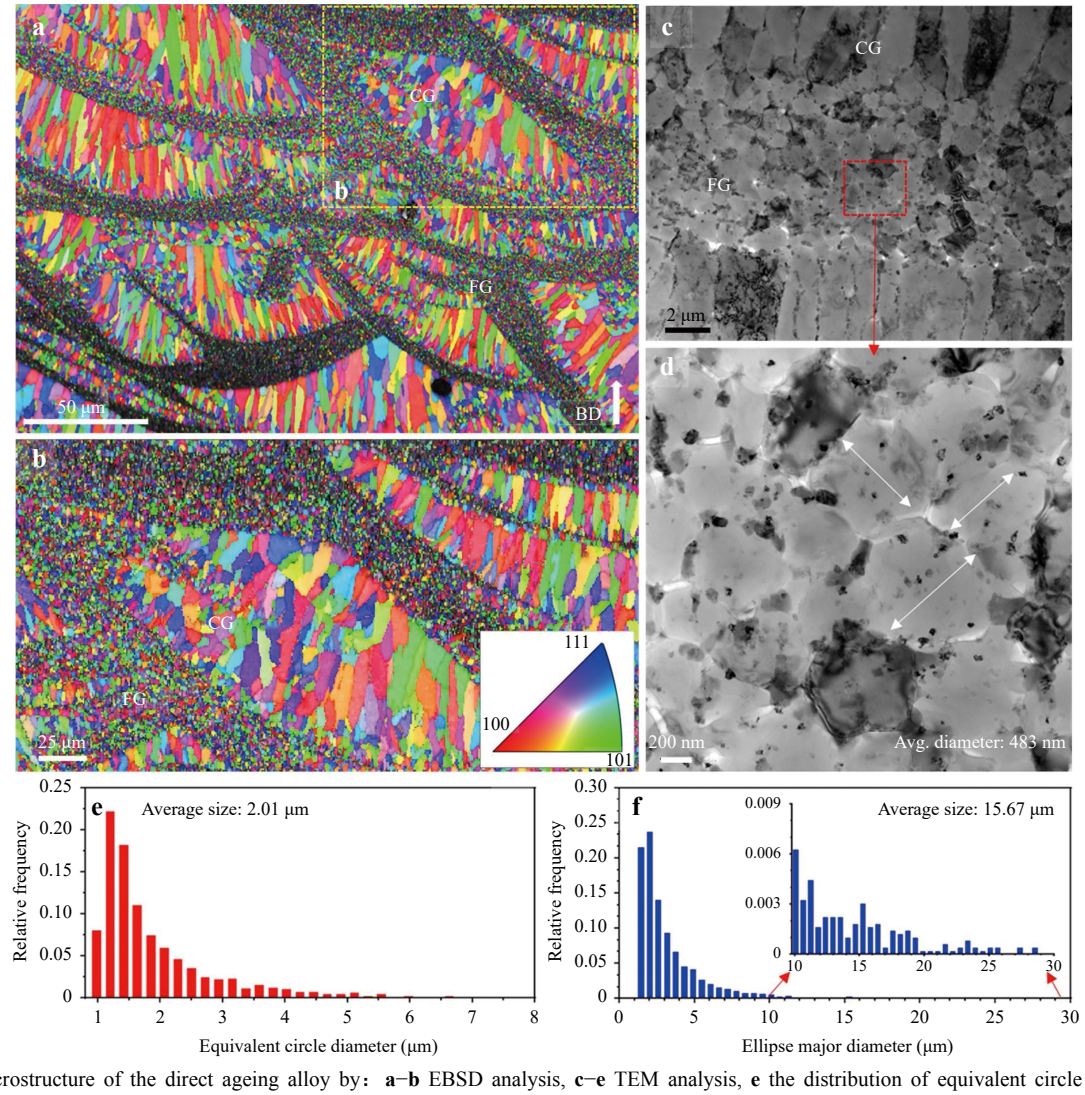

Fig. 4 Microstructure of the direct ageing alloy by: **a**–**b** EBSD analysis, **c**–**e** TEM analysis, **e** the distribution of equivalent circle diameter, showing the grain size, **f** the distribution of ellipse major diameter, showing the grain size.

5 hours, a significant number of precipitates were observed in the matrix as depicted in Fig. 5. These precipitates, which are of nano-scaled size and uniformly distributed between 2-5 nm, exhibit a coherent relationship with the α-Al matrix. Their average grain size is 2.42 ± 0.43 nm, as shown in Fig. 5b, c. Based on the calibration results of selected electron diffraction patterns and the alloy composition analysis, these precipitates are identified as Al_3(Sc, Zr), which possess remarkable precipitation strengthening capabilities. Additionally, an irregular

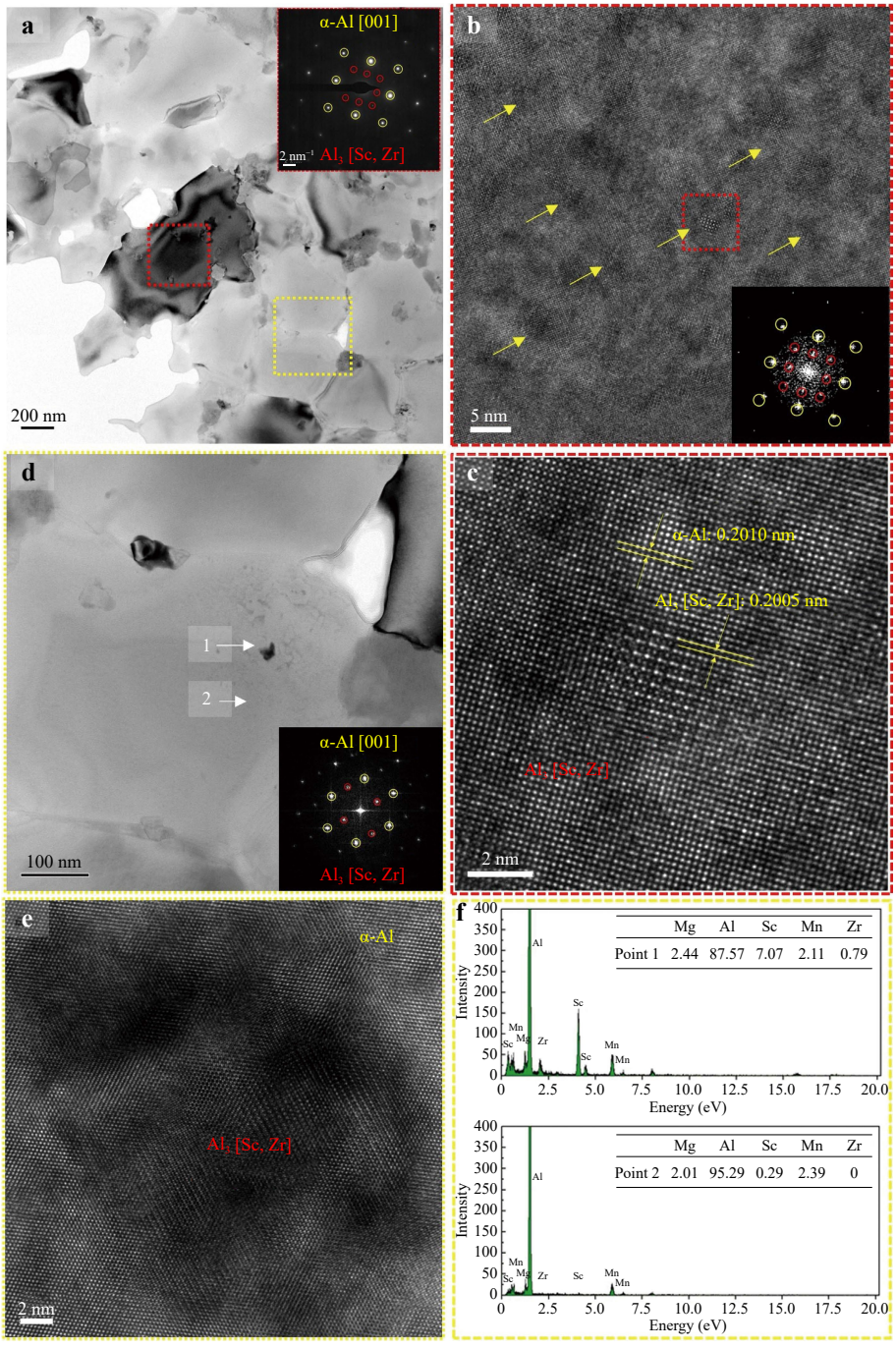

Fig. 5 TEM images of the direct aging alloy: **a** observation area of precipitates; **b** HRTEM image of the Al matrix and the inset is the corresponding FFT of the precipitates; **c** HRTEM image of the precipitates; **d** the primary Al_3(Sc, Zr) phase; **e** HRTEM image of the fine Al_3(Sc, Zr) precipitate, and **f** the corresponding compositions tested by EDS.

secondary phase with a size of 20 nm, much larger than that of the nanoscale precipitates, was observed in the equiaxial core as shown in Fig. 5e, f. The composition analysis of this phase also indicates the presence of Al_3(Sc, Zr). This secondary phase displays a good coherent relationship with the α-Al matrix, indicating that it is the primary Al_3(Sc, Zr) phase, which contributes to the grain refinement effect. The formation of Al_3(Sc, Zr) during solidification of the alloy is attributed to the high concentration of Sc and Zr. It acts as a nucleating agent to refine α-Al grains, thereby contributing to the formation of equiaxial crystal regions.

Mechanical properties

The mechanical properties and fracture toughness of the as-deposited and aged alloys were tested at room temperature. The typical tensile curves are shown in Fig. 6a, while the corresponding values of strength, fracture elongation, and fracture toughness are presented in Fig. 6b. The results indicate that the strength significantly improves after the aging treatment, with the yield strength increasing from 431 MPa to 568 MPa, implying a 32% increase. Moreover, the tensile strength climbed from 467 MPa to 585 MPa, whereas the elongation slightly decreased from 13.5% to 10.3%. Notably, the considerable enhancement in yield strength primarily results from the precipitation strengthening effect of the aged alloy[9]. The direct aging treatment facilitated the precipitation of nano-scaled Al_3(Sc, Zr) dispersed in the Al matrix, leading to a substantial strengthening effect. Prior studies suggest that dispersion strengthening can enhance strength to around 250-300 MPa. However, the direct aging treatment led to a sharp decline in the fracture toughness of the alloy, dropping significantly from 25.1 MPa·√m to 12.3 MPa·√m, as shown in Fig. 6b.

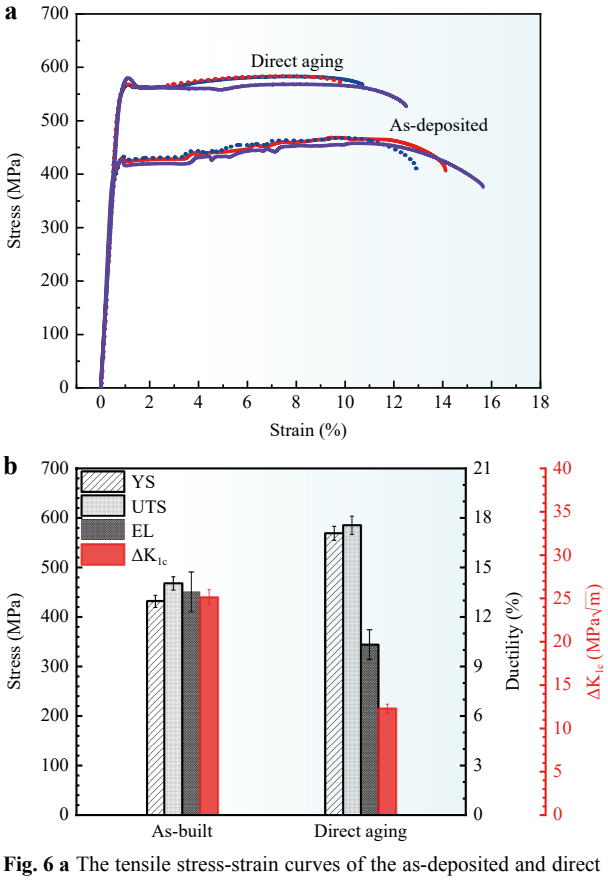

Fig. 6 a The tensile stress-strain curves of the as-deposited and direct aging alloys and **b** the results of the tensile tests and fracture toughness test.

Fig. 7 depicts the tensile fracture morphology of the as-deposited and aged alloys. The fracture surfaces of both alloys display a few micropores, and significant tearing edges are visible on the fracture of the aged alloy. Upon further magnification, it becomes evident that the as-deposited samples exhibit numerous dimples in the fine equiaxed crystal region as well as the columnar crystal region, while the aged samples display more dimples in the former region and fewer in the latter one. These observations imply that both the as-deposited and aged samples exhibit ductile fracture behaviors, although the as-deposited samples display more complete ductility.

Fig. 8 compares the morphology of fracture toughness before and after aging. As depicted in Fig. 8a, the fracture surface consists of two parts, namely the crack initiation region and the ductile fracture region. The fracture morphology reveals that the ductile fracture of the aged alloy is quite smooth and has shallow dimples, indicating a minimal alteration in the direction of the main crack during expansion, resulting in decreased fracture toughness. Conversely, the ductile fracture of the as-deposited alloy is rough, with numerous dimpled surfaces that indicate a consistent alteration in the direction of crack propagation. Therefore, the fracture toughness of the as-deposited alloy is relatively high, which is in agreement with the test results.

High-cycle fatigue testing was conducted on the as-deposited and aged alloys, with loading stress ranging from 180 MPa to 350 MPa. The relationship between loading stress and fatigue cycles is presented in Fig.9. It can be observed that the fatigue cycle initially decreases rapidly and then tends to level off with an increasing loading stress. At 1×10^7 cycle, the loading stress of the as-deposited alloy remained at 180 MPa, indicating its fatigue strength in this work. Similarly, the average fatigue strength of the aged alloy was found to be 220 MPa, witnessing an increase of 16% after direct aging treatment,

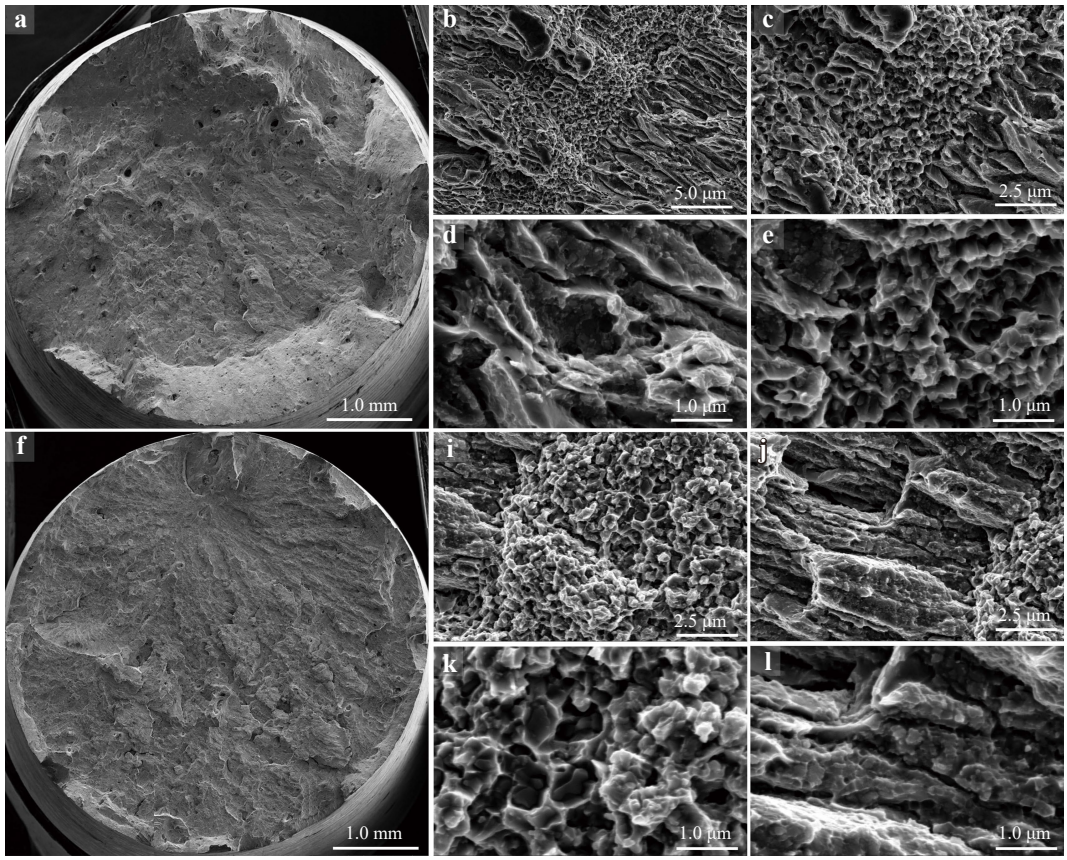

Fig. 7 The tensile fracture morphology of Al-4.5Mn-1.5Mg-0.9Sc-0.2Zr alloys under different tempers: **a**–**e** as-deposited; **f**–**l** direct aging treatment.

even though it is significantly lower than the yield strength increase observed in this work (32%).

Table 2 presents a summary of the mechanical property results, including yield strength (YS), ultimate tensile strength (UTS), elongation (EL), fatigue strength (FS), for the as-deposited and aged alloys at room temperature, along with the calculation of the fatigue strength to yield strength ratio. Generally, aging treatment leads to a substantial increase in yield strength but only a marginal increase in fatigue strength, resulting in an overall decrease in the fatigue strength to yield strength ratio from 40.7% to 38.7%.

Fatigue fracture analysis

To determine key factors contributing to fatigue crack initiation, propagation, and fracture behavior, we analyzed the fatigue fracture characteristics of the as-deposited and directly aged samples. The main characteristics of fatigue fracture are focused on the changes in the crack source and fatigue striations. Fig. 10 illustrates the overall fatigue fracture features in these samples, including changes in fatigue striations during crack propagation. The as-deposited sample was subjected to loading stress of 230 MPa for 141,429 cycles, while the aged sample was subjected to loading stress of 230 MPa for 1,269,524 cycles. Based on the characteristics of fatigue fracture, macroscopic fracture can be divided into three zones: the fatigue crack source zone, fatigue crack propagation zone, and instantaneous fracture zone (as shown in Fig. 10a, f).

From the macroscopic morphology, we observed that the fracture surface of the as-deposited sample was rough and evidenced a shear lip of instantaneous fracture, while the aging specimens had a more uniform and smoother surface. Moreover, the fatigue crack propagation area of the as-deposited sample was significantly larger than the aged sample, aligning with the fracture toughness test results. The as-deposited alloy had greater crack resistance and a larger propagation area compared to the aged alloy. Additionally, we found that the as-deposited alloys had significantly larger fatigue striation spacing in the same region compared to the aged alloys (as shown in Fig. 10b–f and Fig. 10h–l). Some dimples were also observed in the

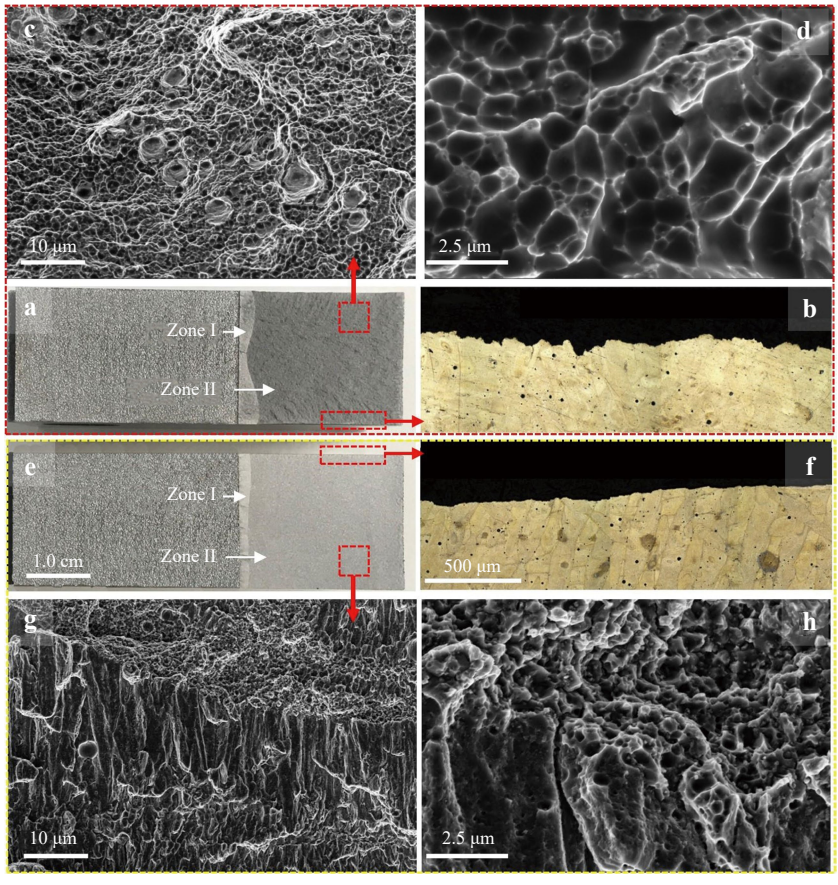

Fig. 8 Fracture toughness surface of various samples: **a**, **e** macroscopic morphology; **b**, **f** lateral morphology; **c**, **d** micro morphology of the fracture toughness of as-deposited specimen; **g**, **h** micro morphology of the fracture toughness of direct aging specimen.

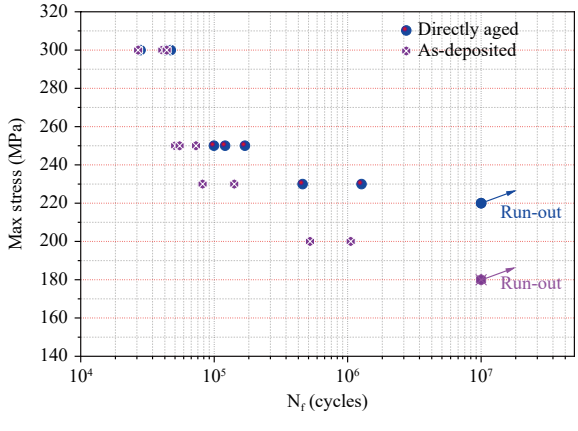

Fig. 9 The relationship between max stress and fatigue cycles of the as-deposited and directly aged alloys

transient fracture zone. The fatigue striation spacing of the aged alloy sample was smaller than that of the as-deposited sample, which we attribute to the high yield strength of the aged alloy sample, resulting in a smaller crack propagation interval during a fatigue cycle. Overall, these results indicate that increasing an alloy's yield strength can reduce the growth rate of fatigue crack and improve its overall fatigue properties.

Table 2 The results of the mechanical properties and fatigue strength test results for the as-deposited and direct aged alloys.

Temper	YS (MPa)	UTS (MPa)	EL (%)	FS (MPa)	FS/YS (%)	ΔK MPa·√m
As-deposited	431	467	13.5	180	40.8%	25.1
Direct aged	568	585	10.3	220	38.7%	12.3

The fatigue crack source is a crucial factor that affects the fatigue life of the alloy. To comprehend the characteristics of the crack source for the Al-4.5Mn-1.5Mg-0.9Sc-0.2Zr alloy, 19 fatigue cracks of the as-deposited and aged samples were scrutinized, and the type and size of the fatigue crack source were determined. Morphology observed by scanning electron microscopy (SEM) and corresponding energy-dispersive X-ray spectroscopy (EDS) was primarily used to determine the type of crack source as depicted in Table 3. The fracture

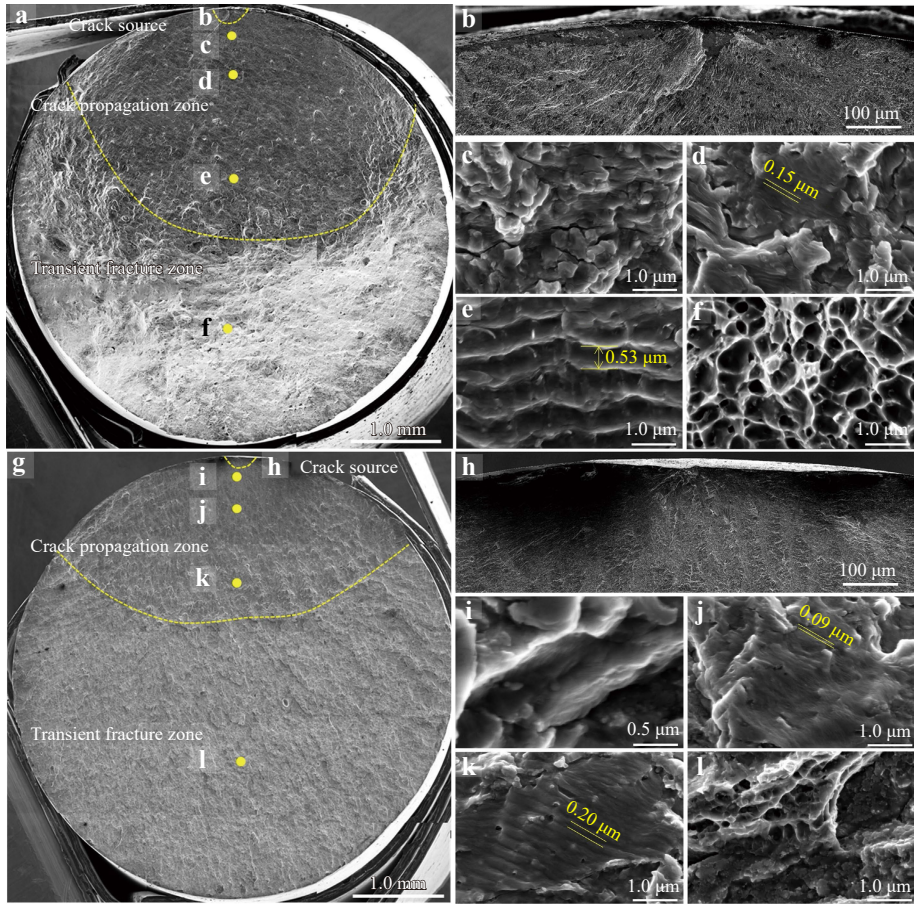

Fig. 10 the fatigue surfaces in the Al-4.5Mn-1.5Mg-0.9Sc-0.2Zr alloys under different tempers: **a**–**f** as-deposited; **g**–**l** direct aging treatment.

morphology near the fatigue crack source of the aged sample is illustrated in Fig. 11, revealing different defect types and sizes. The results obtained from observing the fatigue crack source disclose that Mn-rich phase is the main contributor to fatigue crack initiation, roughly accounting for 60% (Table 3). The second significant cause of fatigue crack initiation is process forming defects such as lack of fusion (LoF) and porosity, which account for 35%. Ultimately, inclusions detected may have originated from splashing powders or raw materials. Furthermore, most of the fatigue crack sources are located on the surface of the sample, while considerably fewer occurrences are detected in the core. Consequently, the outcomes reveal that the initiation of fatigue crack in the Al-4.5Mn-1.5Mg-0.9Sc-0.2Zr alloy is primarily determined by two factors: namely its tendency to form Mn-rich phase, such as Al_6Mn, attributable to the high Mn content, and the defects formed by selective laser melting process, such as non-fusion and porosity.

Discussion

The strengthening mechanisms

The findings demonstrate that the Al-4.5Mn-1.5Mg-0.9Sc-0.2Zr alloy experiences significant enhancement in yield strength following the aging treatment, from 431.0 MPa to 568.0 MPa, which in turn affects its fatigue properties. Thus, it is imperative to investigate the mechanism behind this strengthening phenomenon. The microstructure of the Al-Mn-Sc alloy consists of equiaxed and columnar grains, and the strengthening mechanism involves grain boundary strengthening, solid solution strengthening, and precipitation strengthening. The yield strength of the alloy can be predicted based on the contribution of each strengthening mechanism, according to the following equation:

$$\sigma_{0.2} = \sigma_{GB} + \sigma_{SSS} + \sigma_{ps} \quad (1)$$

where σ_{GB} represent the contribution of grain boundary strengthening, σ_{SSS} represent the contribution of solid

Table 3 HCF test parameters and characteristic parameters of critical defects.

Temper	Number	σ_{max} (MPa)	Crack source		N_f (cycles)
			type	$\sqrt{area}$ (μm)	
As-deposited	#1	300	LoF	45.9	26,909
	#2	300	Pore+LoF	60.9	40,886
	#3	300	Mn-rich phase	34.2	44,067
	#4	250	LoF	40.4	51,024
	#5	250	Mn-rich phase	33.1	73,087
	#6	250	Mn-rich phase	58.2	55,070
	#7	230	LoF	41.8	141,429
	#8	230	Impurity	49.6	81,992
	#9	200	Mn-rich phase	30.5	1,054,146
	#10	200	Mn-rich phase	63.3	522,718
	#11	180	/	/	1.0×10^7
Direct aged	#12	300	LoF	37.3	43,469
	#13	300	Mn-rich phase	24.8	47,189
	#14	300	Pore	49.9	28,027
	#15	250	Mn-rich phase	45.5	160,181
	#16	250	Mn-rich phase	27.3	120,712
	#17	250	Mn-rich phase	46.0	169,887
	#18	250	Impurity	69.1	99,411
	#19	230	Mn-rich phase	89.1	460,126
	#20	230	Pore+LoF	50.9	1,269,524
	#21	220	/	/	1.0×10^7
	#22	220	/	/	1.0×10^7

solution strengthening, and σ_{ps} represents the contribution of precipitation strengthening.

Firstly, the Al-Mn-Sc alloy is comprised of fine equiaxed and columnar grains, resulting in grain boundary strengthening that is influenced by both coarse and fine grains. This can be determined using the following Eq. 12:

$$\sigma_{GB} = \sigma_o + \alpha \frac{k}{\sqrt{d_1}} + (1-\alpha)\frac{k}{\sqrt{d_2}} \quad (2)$$

where σ_o is the friction stress of pure aluminum (approximately 20 MPa), k is the Hall-Petch coefficient (taken as 0.17 MPa·$m^{1/2}$ from Ref. 26). α is the area fraction of fine equiaxed grains (47% in this study based on EBSD statistics), d_1 is the average size of equiaxed grains with a value of about 0.483μm and d_2 is the average size of columnar grain with a value of roughly 2.01 μm. The resulting yield strength increment due to grain boundary strengthening is approximately 185.1 MPa.

Secondly, considering that Sc and Zr are mainly used to form precipitates, the solution strengthening of the alloy mainly comes from Mn and Mg, and the contribution of solid solution strengthening can be calculated as below[27]:

$$\sigma_{SSS} = \sum_i A_i C_i^{\beta_i} \quad (3)$$

where $A_i$represents the solid solution strengthening constants of the various solute elements (mainly Mn and Mg), $C_i$represents the concentrations of the various solute species and β_i represents the power law coefficient for each solute species. Based on Eq. 3, the yield strength improvement due to solid solution strengthening of Mn and Mg is estimated to be 121.0 MPa.

Finally, the precipitation strengthening of the alloy mainly comes from the precipitation of nano-scale phase Al_3(Sc, Zr). The strengthening effect is related to the size and volume fraction of the precipitated phase. The contribution of precipitation strengthening can be calculated as below[28].

$$\sigma_{ps} = \sigma_{ms} + \sigma_{cs} \quad (4)$$

where σ_{ms} is the modulus mismatch strengthening, and σ_{cs} is the coherency strengthening. Compared to the previous study[29], the investigated alloy possesses a similar composition and underwent the same aging treatment. Both the alloys exhibit comparable precipitate size, indicating similar levels of precipitation strengthening. The value of σ_{ms} is approximately 228MPa, while σ_{cs} is around 50MPa. Consequently, the value of σ_{ps} is estimated to be around 278MPa.

In brief, the calculated yield strength is approximately 585.1 MPa, which is approximately 3% greater than the experimental result of 568.0 MPa. The likely explanation for this discrepancy is that the calculation of solid solution strengthening assumes that both Mn and Mg are completely dissolved within the aluminum matrix. However, in reality, some Mn atoms are present at the grain boundaries in the form of Mn-rich phases, resulting in a higher calculated yield strength.

Fatigue strength and its influencing factors

The results of high-cycle fatigue tests indicate that the fatigue strength of the Al-4.5Mn-1.5Mg-0.9Sc-0.2Zr alloy is 180 MPa and 220 MPa, respectively. Fig. 12 compares the fatigue strength and tensile strength of high-strength aluminum alloys (Al-Mg-Sc and Al-Mn-Sc) and Al-Si alloys prepared by selective laser melting. It is noteworthy that the fatigue strength of the Al-Mn-Sc alloy (220 MPa) is higher than that of the Al-Mg-Sc alloy (200 MPa) without hot isostatic pressing treatment[24], and the average fatigue strength of the Al-Sc alloys (~200 MPa) is higher than that of the Al-Si alloys (~100 MPa). This can be

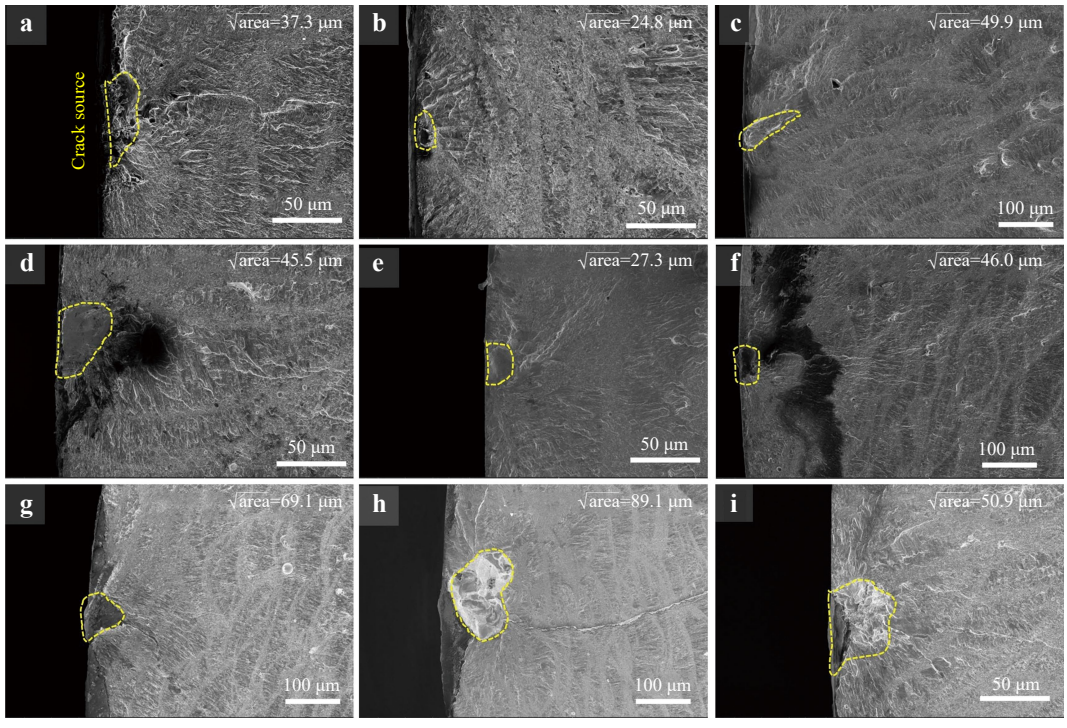

Fig. 11 Fatigue crack sources of the aged alloys under different loading stress conditions: the max stress and cycle number are as following **a** 300 MPa, N_f=47,189; **b** 300 MPa, N_f=43,469; **c** 300 MPa, N_f=28,027; **d** 250 MPa, N_f=160,181; **e** 250 MPa, N_f=120,712; **f** 250 MPa, N_f=99,411; **g** 250 MPa, N_f=169,887; **h** 230 MPa, N_f=460,126; **i** 230 MPa, N_f=1,269,524.

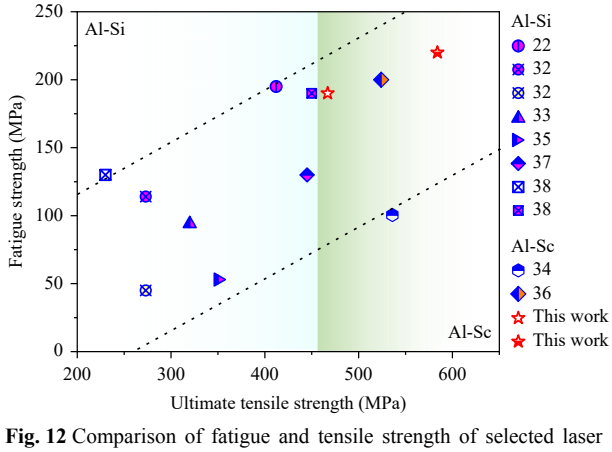

Fig. 12 Comparison of fatigue and tensile strength of selected laser melted aluminum alloys including Al-Si, Al-Mg-Mn-Sc-Zr and Al-Mn-Mg-Sc-Zr[22, 32-38].

attributed to the high tensile strength as it is a major determinant of the intrinsic fatigue limit of the material[30,31].

However, despite the high tensile strength of our aluminum alloy, the proportion of as-deposited and aged fatigue strength and yield strength is only 41.8% and 35.2%, respectively, which is significantly lower than that of the AlSi7Mg alloy (63.7%) and the AlSi10Mg alloy (58.1%). It is evident that the fatigue strength of the Al-4.5Mn-1.5Mg-0.9Sc-0.2Zr alloy is relatively low, and fatigue fracture results indicate that Mn-rich phase, unfused material, and porosity defects in the alloy are the key causes of fatigue initiation, with the proportion of samples caused by Mn-rich phase fatigue initiation reaching 50%. In comparison, the fatigue initiation of Al-Si alloy is mainly due to process defects, and it is inferred that, compared to the crack initiation source of Al-Si alloy, Al-4.5Mn-1.5Mg-0.9Sc-0.2Zr has more factors that induce crack initiation, resulting in significantly lower fatigue properties. For example, the Al-Mg-Sc-Zr alloy, in the absence of Mn-rich phase as the crack source, has a fatigue strength as high as 340 MPa after hot isostatic pressing treatment, and the ratio to tensile strength is 65.4%[24].

Following direct aging heat treatment of the Al-4.5Mn-1.5Mg-0.9Sc-0.2Zr alloy, a significant number of nano-scaled Al_3(Sc, Zr) phases became dispersed in the aluminum matrix, resulting in notable precipitation strengthening. As a result, the yield strength of the alloy elevated from 431 MPa to 568 MPa. Nonetheless, the influence of direct aging treatment on the process defects and the Mn-rich phase in the alloy's microstructure is minor. The Mn-rich phase is the primary phase that precipitates at a high temperature during the solidification

process, and the aging temperature is 300 ℃. Fatigue fracture analysis demonstrates that an increase in the yield strength reduces the fatigue striation spacing, postpones the fatigue expansion rate through the variant phase, enhances the fatigue performance, and improves the alloy's fatigue strength.

The relationship between fatigue strength and defect size

The fatigue strength of selective laser melted aluminum alloys generally increases with rising tensile strength. However, internal defects in the alloy, such as non-fusion, pores, and related secondary phase factors, have a controlling influence on fatigue strength. It is necessary to assess the fatigue performance of a given volume of LPBF material on the basis of the largest probable defects formed. according to previous research, the impact of defects on the fatigue limit can be predicted by adopting the K-T diagram approach.

The K-T diagram described using El-Haddad model based on the $\sqrt{area}$ parameter can be further depicted as below[39,40]:

$$\Delta\sigma_w = \Delta\sigma_{w0}\sqrt{\frac{\sqrt{area_0}}{\sqrt{area}+\sqrt{area_0}}} \tag{5}$$

where $\Delta\sigma_w$ is the stress range or fatigue limit, and $\sqrt{area}$ is the defect size. $\sqrt{area_0}$ represents the material intrinsic defect size. The intrinsic defect size is closely related to the microstructure of the material. According to the research results in reference[24], their intrinsic defect size of Al-Mg-Sc-Zr is approximately equal to the length of columnar grains. Since the Al-Mn-Sc and Al-Mg-Sc-Zr alloys have similar microstructure, and the columnar grain length of Al-Mn-Sc alloy is approximately 15.67 μm, the intrinsic defect length is 15.67 μm. Additionally, it is noteworthy that $\Delta\sigma_{w0}$ represents the fatigue limit of a given volume without defects, and it is a purely theoretical estimation for an ideal material. Pang et al.[31] proposed an empirical model to estimate the fatigue limit based on the microstructure and tensile properties as:

$$\sigma_w = C\cdot\sigma_b - D\cdot\sigma_b^2 \tag{6}$$

where σ_w is the basis fatigue limit under R = −1; C is intrinsic factor and D is fatigue sensitivity coefficient to assumed defects. σ_b=585 MPa is the ultimate tensile strength for the studied alloys. Here C=0.53 indicates the impact without defects and D = 0 for Al alloys[31]. Considering the stress ratio, a value of $\Delta\sigma_{w0}$ = 407 MPa was obtained through the Walker equation when R = 0.1[41].

From the above calculation results, the El-Haddad model can be obtained, as shown in the red curve in Fig. 13.

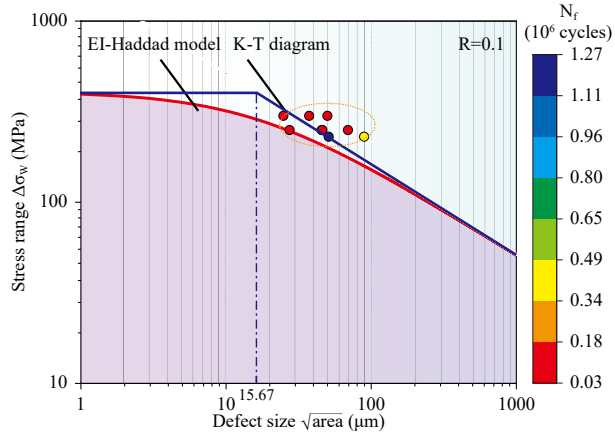

Fig. 13 Relationship between defect size and fatigue strength of the aged Al-4.5Mn-1.5Mg-0.9Sc -0.2Zr alloy.

Moreover, based on the relationship between the intrinsic defect size and the crack growth threshold, the ΔK_{th} of Al-Mn-Sc alloys can be evaluated as follows:

$$\sqrt{area_0} = \frac{1}{\pi}\left(\frac{\Delta K_{th}}{F_w\Delta\sigma_{w0}}\right)^2 \tag{7}$$

where F_w is the Murakami geometry factor for near-surface defects and the value is 0.65. According to the Eq. 7, the long crack growth threshold ΔK_{th} was calculated, with a value of 1.86 MPa·√m, which is closed to 2.0 MPa·√m[24].

Based on the fatigue limit and crack growth threshold of a defect-free volume, an enhanced K-T diagram can be constructed, represented by the blue line in Fig. 13. It is apparent that all failures occur above the El-Haddad curve, and the greater the distance from the curve, the shorter the fatigue life of the specimens. The K-T diagram offers a quantitative correlation between defect size and fatigue limit, allowing for fatigue limit prediction in terms of material defects. For the aged Al-4.5Mn-1.5Mg-0.9Sc-0.2Zr alloy, the surface defect size is approximately 47.2 μm and the fatigue strength is about 220 MPa, nearly aligning with predicted fatigue strength of 205 MPa by the K-T diagram.

On the one hand, previous research results and K-T diagrams indicate that 3D printed Al-Sc alloys are prone to defects, and their fatigue strength is highly sensitive to defect size. Thus, optimizing the printing process parameters and hot isostatic pressing treatment is essential to adjust defect size and enhance fatigue strength[42]. On the other hand, for Al-Mn-Sc alloys, the Mn-rich phase is a significant factor as a fatigue crack source, and alloy design should begin by appropriately adjusting Mn content. Further optimization is necessary, such as reducing the Mn content, decreasing the number of Mn-rich phases, and

refining their size. The Mn-rich phase forming during the melting process would create a micron-scaled second phase that has minimal effect on strength and ductility but tremendous fatigue properties, necessitating future research in this area.

Conclusions

This study examined the microstructure, mechanical characteristics, and fatigue properties of the selective laser melted Al-4.5Mn-1.5Mg-0.9Sc-0.2Zr alloy in both the as-deposited and directly aged states. Through fracture and statistical analysis of fatigue crack sources, the primary components responsible for fatigue were identified. Additionally, the study investigated the impact of yield strength improvement on the crack propagation process. The findings of this research are presented as follows:

1) Direct aging treatment significantly improves the overall mechanical properties of the alloy studied, with an increase in yield strength from 431 MPa to 568 MPa, tensile strength from 467 MPa to 585 MPa, and an elongation of more than 10% achieved. The substantial increase in strength is attributed to the precipitation of nano-scaled Al_3(Sc, Zr) during the aging process, resulting in considerable strengthening by aging.

2) The fatigue strength of the alloy increases from 180 MPa to 220 MPa after direct aging treatment. The aging treatment enhances the yield strength, leading to a decrease in the rate of fatigue crack propagation and an increase in fatigue strength. However, the increase in fatigue strength is only 16%, considerably less than the 32% increase in alloy yield strength.

3) The major causes of fatigue fracture in the alloy studied are the Mn-rich phase, and the absence of fusion flaws and porosity defects. It is challenging to prevent the onset of fatigue cracks because the direct aging temperature (300 °C) has a minimal effect on these two types of defects. However, an increase in yield strength impedes fatigue crack propagation. Therefore, direct aging treatment can enhance the alloy's fatigue performance to a certain extent.

4) Based on the microstructure characteristics and mechanical properties of Al-4.5Mn-1.5Mg-0.9Sc-0.2Zr alloy, the relationship between defect size and fatigue strength of the alloy was established, and an EI model was obtained, that is, $\Delta\sigma_w = 407 \cdot \sqrt{15.67/(\sqrt{area} + 15.67)}$. Using this model, the fatigue strength can be better predicted according to the defect size, which is in good agreement with the experimental results. The crack growth threshold of this alloy was also predicted, with a value of 1.86 MPa·√m.

Acknowledgements

This work was financially supported by Ji Hua Laboratory "Development of additive manufactured core process and special equipment for key parts of aero-engines" (No. X190351TM190) and the Basic and Applied Basic Research Foundation of Guangdong Province (No. 2022A1515011597).

Author details

[1]Institute of Advanced Additive Manufacturing, Ji Hua Laboratory, Foshan, Guangdong, 528200, China. [2]Department of Mechanical Engineering, College of Engineering, Shantou University, Shantou, Guangdong, 515063, China. [3]School of Materials Science and Engineering, Northeastern University, Shenyang 110819, China

Author contributions

Huaping Tang: Conceptualization, Investigation, & Writing-original draft. Chaofeng Gao: Methodology & Funding acquisition. Shiheng Zhang: Writing-review & editing. Xiaojing Xiong: Testing and raw material preparation. Sheng Cao: Writing-review & editing. Xiaopeng Wu: Preparation of test samples. Yunjie Bi: Writing -review & editing. Jeremy Heng Rao: Supervision, Writing -review & editing.

Conflict of interest

The authors have no competing interests to declare.

Received: 02 August 2023 Revised: 21 November 2023 Accepted: 23 November 2023

Published online: 24 January 2024

References

1. Aboulkhair, N. T. et al. 3D printing of Aluminium alloys: Additive Manufacturing of Aluminium alloys using selective laser melting. *Progress in Materials Science* **106**, 100578 (2019).
2. Deng, Q. W. et al. One droplet toward efficient alcohol detection using femtosecond laser textured micro/nanostructured surface with superwettability. *Small Methods* **7**, 2300290 (2023).
3. Huang, Q. Q. et al. Femtosecond laser-scribed superhydrophilic/superhydrophobic self-splitting patterns for one droplet multi-detection. *Nanoscale* **15**, 11247-11254 (2023).
4. Wang, L. X. et al. Wetting ridge-guided directional water self-transport. *Advanced Science* **9**, 2204891 (2022).
5. Bayoumy, D. et al. The latest development of *Sc*-strengthened aluminum alloys by laser powder bed fusion. *Journal of Materials Science & Technology* **149**, 1-17 (2023).
6. Tang, H. P. et al. Effects of direct aging treatment on microstructure, mechanical properties and residual stress of selective laser melted AlSi10Mg alloy. *Journal of Materials Science & Technology* **139**, 198-209 (2023).
7. Martin, J. H. et al. 3D printing of high-strength aluminium alloys. *Nature* **549**, 365-369 (2017).
8. Sun, T. T. et al. The role of *in-situ* nano-TiB_2 particles in improving the printability of noncastable 2024Al alloy. *Materials Research Letters* **10**, 656-665 (2022).
9. Wang, K. D. et al. Effect of adding methods of nucleating agent on microstructure and mechanical properties of Zr modified Al-Cu-Mg alloys prepared by selective laser melting. *Acta Metallurgica Sinica* **58**, 1281-1291 (2022).
10. Shi, Y. J. et al. Effect of platform temperature on the porosity, microstructure and mechanical properties of an Al-Mg-Sc-Zr alloy fabricated by selective laser melting. *Materials Science and Engineering:A* **732**, 41-52 (2018).

11. Cordova, L. et al. Effects of powder reuse on the microstructure and mechanical behaviour of Al-Mg-Sc-Zr alloy processed by laser powder bed fusion (LPBF). *Additive Manufacturing* **36**, 101625 (2020).
12. Jia, Q. B. et al. Selective laser melting of a high strength Al-Mn-Sc alloy: Alloy design and strengthening mechanisms. *Acta Materialia* **171**, 108-118 (2019).
13. Jia, Q. B. et al. Precipitation kinetics, microstructure evolution and mechanical behavior of a developed Al-Mn-Sc alloy fabricated by selective laser melting. *Acta Materialia* **193**, 239-251 (2020).
14. Zhang, J. L. et al. A novel crack-free Ti-modified Al-Cu-Mg alloy designed for selective laser melting. *Additive Manufacturing* **38**, 101829 (2021).
15. Bi, J. et al. An additively manufactured Al-14. *1Mg-0. 47Si-0. 31Sc-0. 17Zr alloy with high specific strength, good thermal stability and excellent corrosion resistance. Journal of Materials Science & Technology* **67**, 23-35 (2021).
16. Li, R. D. et al. Developing a high-strength Al-Mg-Si-Sc-Zr alloy for selective laser melting: Crack-inhibiting and multiple strengthening mechanisms. *Acta Materialia* **193**, 83-98 (2020).
17. Zhao, J. H. et al. Selective laser melting Al-3. *4Mg-0. 5Mn-0. 8Sc-0. 4Zr alloys:From melting pool to the microstructure and mechanical properties. Materials Science and Engineering:A* **825**, 141889 (2021).
18. Zhou, S. Y. et al. Selective laser melting additive manufacturing of 7xxx series Al-Zn-Mg-Cu alloy: Cracking elimination by co-incorporation of Si and TiB_2. *Additive Manufacturing* **36**, 101458 (2020).
19. Wang, J. H. et al. A crack-free and high-strength Al-Cu-Mg-Mn-Zr alloy fabricated by laser powder bed fusion. *Materials Science and Engineering:A* **854**, 143731 (2022).
20. Li, L. B. et al. Microstructures and tensile properties of a selective laser melted Al-Zn-Mg-Cu (Al7075) alloy by Si and Zr microalloying. *Materials Science and Engineering:A* **787**, 139492 (2020).
21. Michi, R. A. et al. Towards high-temperature applications of aluminium alloys enabled by additive manufacturing. *International Materials Reviews* **67**, 298-345 (2022).
22. Nasab, M. H. et al. Effect of surface and subsurface defects on fatigue behavior of AlSi10Mg alloy processed by laser powder bed fusion (L-PBF). *Metals* **9**, 1063 (2019).
23. Defanti, S. & Bassoli, E. Repeatability of the fatigue performance of additively manufactured A357. *0 under different thermal treatment conditions. Materials Science and Engineering:A* **805**, 140594 (2021).
24. Schimbäck, D. et al. Deformation and fatigue behaviour of additively manufactured Scalmalloy® with bimodal microstructure. *International Journal of Fatigue* **172**, 107592 (2023).
25. Shen, X. F. et al. Effect of heat treatments on the microstructure and mechanical properties of Al-Mg-Sc-Zr alloy fabricated by selective laser melting. *Optics & Laser Technology* **143**, 107312 (2021).
26. Croteau, J. R. et al. Microstructure and mechanical properties of Al-Mg-Zr alloys processed by selective laser melting. *Acta Materialia* **153**, 35-44 (2018).
27. Gypen, L. A. & Deruyttere, A. Multi-component solid solution hardening - Part 1 proposed model. *Journal of Materials Science* **12**, 1028-1033 (1977).
28. Fuller, C. B., Seidman, D. N. & Dunand, D. C. Mechanical properties of Al(Sc, Zr) alloys at ambient and elevated temperatures. *Acta Materialia* **51**, 4803-4814 (2003).
29. Bayoumy, D. et al. Origin of non-uniform plasticity in a high-strength Al-Mn-Sc based alloy produced by laser powder bed fusion. *Journal of Materials Science & Technology* **103**, 121-133 (2022).
30. Rao, J. H. et al. Improving fatigue performances of selective laser melted Al-7Si-0. *6Mg alloy via defects control. International Journal of Fatigue* **129**, 105215 (2019).
31. Pang, J. C. et al. General relation between tensile strength and fatigue strength of metallic materials. *Materials Science and Engineering:A* **564**, 331-341 (2013).
32. Wu, Z. K. et al. The effect of defect population on the anisotropic fatigue resistance of AlSi10Mg alloy fabricated by laser powder bed fusion. *International Journal of Fatigue* **151**, 106317 (2021).
33. Aboulkhair, N. T. et al. Improving the fatigue behaviour of a selectively laser melted aluminium alloy: Influence of heat treatment and surface quality. *Materials & Design* **104**, 174-182 (2016).
34. Qin, Z. H. et al. Anisotropic high cycle fatigue property of Sc and Zr-modified Al-Mg alloy fabricated by laser powder bed fusion. *Additive Manufacturing* **49**, 102514 (2022).
35. Boniotti, L. et al. Experimental and numerical investigation on compressive fatigue strength of lattice structures of AlSi7Mg manufactured by SLM. *International Journal of Fatigue* **128**, 105181 (2019).
36. Schimbäck, D. et al. An improved process scan strategy to obtain high-performance fatigue properties for Scalmalloy®. *Materials & Design* **224**, 111410 (2022).
37. Yan, Q., Song, B. & Shi, Y. S. Comparative study of performance comparison of AlSi10Mg alloy prepared by selective laser melting and casting. *Journal of Materials Science & Technology* **41**, 199-208 (2020).
38. Baek, M. S. et al. Influence of heat treatment on the high-cycle fatigue properties and fatigue damage mechanism of selective laser melted AlSi10Mg alloy. *Materials Science and Engineering:A* **819**, 141486 (2021).
39. Beretta, S. & Romano, S. A comparison of fatigue strength sensitivity to defects for materials manufactured by AM or traditional processes. *International Journal of Fatigue* **94**, 178-191 (2017).
40. El Haddad, M. H., Topper, T. H. & Smith, K. N. Prediction of non propagating cracks. *Engineering Fracture Mechanics* **11**, 573-584 (1979).
41. Dowling, N. E., Calhoun, C. A. & Arcari, A. Mean stress effects in stress-life fatigue and the Walker equation. *Fatigue & Fracture of Engineering Materials & Structures* **32**, 163-179 (2009).
42. Cao, S. et al. Review of laser powder bed fusion (LPBF) fabricated Ti-6Al-4V: process, post-process treatment, microstructure, and property. *Light:Advanced Manufacturing* **2**, 313-332 (2021).